Kinetic Pathways of Order-to-Order Phase Transitions in Block Copolymer Films under an Electric Field

K. S. Lyakhova,[†] A. V. Zvelindovsky,*[,‡] and G. J. A. Sevink*[,§]

Polymer Physics, Eindhoven University of Technology, PO Box 513, a2.40, 5600 MB Eindhoven, The Netherlands; Centre for Materials Science, Department of Physics, Astronomy and Mathematics, University of Central Lancashire, Preston, PR1 2HE, United Kingdom; and Leiden Institute of Chemistry, Leiden University, PO Box 9502, 2300 RA Leiden, The Netherlands

Received January 20, 2006

ABSTRACT: We study kinetic pathways of phase transitions in thin films of block copolymers subjected to an applied electric field by means of dynamic self-consistent-field calculations. We consider structures ranging from spheres to lamellae. We find that the kinetic pathway taken by a system near a phase transition is very different from the one far from a phase transition.

I. Introduction

Block copolymers are fascinating materials capable of forming a large variety of soft nanostructures depending on the chemical composition of blocks and the architecture of relatively simple molecules.[1] A challenging task for the application of block copolymers in nanomanufactured devices is to form perfect arrays of nanostructures. One possible way to do so is by the application of an external field to a block copolymer sample. Examples of such fields commonly used in experimental practice are shear flow,[1,2] electric field,[3−6] and temperature gradients.[7]

Often experimental samples are thin films.[8] Recently we have shown that the phase behavior of cylinder-forming block copolymers in thin films is extremely complex even without external fields like shear and electric fields.[9] Both the transition dynamics and the equilibrium behavior in the experimental situation are found to be well explained by means of dynamic self-consistent-field theory.[9−12] We note that both in our calculations and in the experiments the observed equilibrium behavior may represent long-living metastable phases and can therefore differ from theoretical predicted equilibrium phases.

In the presence of an electric field, an orientation of microdomains parallel to the external electric field is energetically favored due to the different dielectric properties of the two blocks. For lamellar and cylindrical systems this effect counteracts any interfacial alignment due to preferential attraction to the electrode surfaces. For spherical systems, this effect leads to an elongating of the spheres in the direction of the electric field.

Several theoretical groups have studied electric-field-induced orientational and order-to-order phase transitions[13−21] and compared with experiments.[22−27] Most of the theoretical analysis is based on the calculation of an extra contribution to the free energy due to electrostatics for different orientation of structures and then comparing the energies of the static patterns. As to the dynamic behavior, Onuki and Fukuda examined the dynamics of lamellar undulation instability induced by the electric field.[15] To answer the question *how* a phase transition proceeds further in time, one needs to develop an approach to examine the dynamics of the pattern evolution. Recently, such a method has been proposed[28] for a block copolymer system under an electric field. It employs an approximation to the model in ref 29. The authors of ref 29 were the first who numerically solve the Maxwell equation for polymer melts under electric field.

In contrast to most of the static theoretical studies, experimental studies have intrinsically considered the dynamics pathways of electric-field-induced phase transitions.[30−33] Since direct observation of the three-dimensional structural evolution details is not within reach of most experimental methods, they often focus on the kinetics of average structural properties or the time scales at which a transition takes place. It was observed that the initial stage of the process history prior to the application of an electric field is an important factor in the transition kinetics. When a block copolymer system is not or poorly microphase separated prior to the application of the electric field, composition fluctuations can already be oriented by the electric field,[22] and the orientation of microdomains takes place directly after cooling through the order−disorder temperature. In an initially ordered system the rearrangement dynamics depends on the defect density[23] and on the degree of microphase separation,[26] which determine the growth of undulation instability to a great extent. Here *the degree of microphase separation* simply denotes the strength of A−B blocks interaction in A−B block copolymers (in theoretical studies, the value of χN), leading to various microstructures like spheres, cylinders, lamellae, etc. We will use this notion in the remainder of the paper.

An electric-field-induced thin film sphere-to-cylinder (S-to-C) transition was observed experimentally by Ting et al.[27] for a sphere-forming system. In this system, cross-sectional TEM snapshots of the intermediate stages of the alignment process indicated that spherical microdomains were first deformed in ellipsoids under an electric field and then interconnect in cylindrical microdomains oriented in the direction of electric field.

Electric-field-induced reorientation of a cylinder-forming block copolymer ($C_{||}$-to-$C_{\perp}$) was studied by Thurn-Albrecht et al.[25,32] for different initial situations. The electric field was found to orient composition fluctuations in the disordered state, resulting in a preferred growth of oriented nuclei. An electric field applied to a microphase-separated copolymer led to a disruption of grains into smaller pieces that were able to rotate.

[†] Eindhoven University of Technology.
[‡] University of Central Lancashire.
[§] Leiden University.

10.1021/ma060143r CCC: $33.50
Published on Web 03/16/2006

This disruption occurred via the growth of undulations at the cylinder interfaces.

For lamellae forming block copolymer the electric-field-induced alignment kinetics has been studied by many groups. Amundsen et al.[23,24] proposed two mechanisms: selective electric-field-induced disordering and alignment through movements of defects. Only the latter mechanism was supported by their experiments, and the fundamental process was found to be the movement of edge dislocations.[24] In ref 33 an in-situ SAXS alignment study of an ordered lamellar block copolymer melt in an electric field was found to indicate that reorientation of lamellar domains goes via a disruption or disordering of the original structure, leading to a substantial loss of long-range order. In the intermediate stage the system tends to reduce the grain sizes so the rotation of domains can occur. Similarly, Ting et al.[31] showed that the dominant mechanism is one where lamellae are locally disrupted and reappear in the direction of the applied field. Böker et al.[30] identified two distinct microscopic mechanisms of electric-field-induced $L_{||}$-to-$L_{\perp}$ transition in a concentrated diblock copolymer solution: nucleation and growth of domains and grain rotation. This behavior was initially attributed to the difference in viscosity due to the different solvent concentrations. It was later argued[26,28,34] that viscosity may play a role but that these mechanisms are intrinsic to the degree of microphase separation of the system.

The objective of this work is to consider the detailed kinetic transition pathways of order-to-order (S) and orientational (C and L) phase transitions induced by an electric field and to identify unifying mechanisms.

II. Model

Dynamic self-consistent-field theory is used to describe the block copolymer system.[36,39] The time evolution of the system is modeled by diffusion dynamics

$$\frac{\partial \rho_I}{\partial t} = M\nabla^2 \mu_I + \eta_I \tag{1}$$

where ρ_I is the concentration of blocks of type I, which has dimensions of inverse volume, μ_I is chemical potential, M is constant mobility, and η_I is thermal noise, which is related to M via the fluctuation−dissipation theorem.[36] An extensive description of relevant dynamical models can be found in ref 37. We use the most simple model for M, which is just a constant. A more elaborate model can be found in ref 38. The chemical potential $\mu_I = \delta F/\delta \rho_I$ can be found from the free energy:[36,39]

$$F^0[\rho] = -kT \ln\left(\frac{\Phi^n}{n!}\right) - \sum_I \int_V U_I(\mathbf{r})\, \rho_I(\mathbf{r})\, d\mathbf{r} + \frac{1}{2}\sum_{I,J} \int_{V^2} \epsilon_{IJ}(|\mathbf{r}-\mathbf{r}'|)\, \rho_I(\mathbf{r})\, \rho_J(\mathbf{r}')\, d\mathbf{r}\, d\mathbf{r}' + \sum_I \int_{V^2} \epsilon_{IM}(|\mathbf{r}-\mathbf{r}'|)\, \rho_I(\mathbf{r})\, \rho_M(\mathbf{r}')\, d\mathbf{r}\, d\mathbf{r}' + \frac{\kappa}{2}\int_V \Big(\sum_I \rho_I(\mathbf{r}) - \rho_I^0\Big)^2 d\mathbf{r} \tag{2}$$

where nought at F indicates that the free energy is calculated for the system in the absence of any external fields. The Boltzmann constant is denoted by k, T is the temperature, n is the number of polymer molecules in the volume V occupied by the system, and Φ is the intramolecular partition function for ideal polymer chains. The parameter κ determines the compressibility of the system, and ρ_I^0 is the mean concentration of the I-block (where the average is taken over the sample volume V). For $\kappa \to \infty$ the system becomes incompressible. The external potentials U_I and the concentration fields ρ_I are related via the density functional.[36] The polymer chains are modeled as so-called Gaussian chains, where the single-chain Hamiltonian describes a set of connected harmonic springs:

$$H = kT\frac{3}{2a^2}\sum_{s=2}^{N}(\mathbf{R}_s - \mathbf{R}_{s-1})^2 \tag{3}$$

with a being the Gaussian chain bond length, N the number of beads in the chain, and $\mathbf{R}_s$ the coordinate of bead s. The time evolution of the system as described by eq 1 assumes that the system is in quasi-equilibrium, so that there exists a free energy functional, eq 2. This free energy functional does not explicitly depend on time. On every time instance of the systems evolution, eq 1, all intramolecular degrees of freedom are assumed to be equilibrated. This is a good approximation in case that the internal dynamics of a single chain is faster than the collective dynamics of the ensemble of chains. Although the free energy description, eq 2, incorporates spatial resolution on the level of beads of chains, the time evolution described by eq 1 is coarse-grained, and the smallest physical volume entering it is the volume of a single polymer chain v. We use this volume to introduce a dimensionless variable $\psi = v(\rho_A - \rho_A^0)$. Here A stands for A-blocks. One variable is sufficient in the case of incompressible copolymer melts with only two block types, which we will consider in the remainder of the paper. Therefore, we will drop the subscripts for block types. The variable ψ is an order parameter, which is the local deviation of the volume fraction of blocks A from their uniform distribution. It is small for weakly segregated systems.

In the presence of an electric field $\mathbf{E}(\mathbf{r})$ the chemical potential can be split into two terms:[40]

$$\mu = \mu^0 + \mu^{el}, \quad \xi = \frac{\mu^{el}}{v} = -\frac{E^2}{8\pi}\frac{\partial \epsilon}{\partial \psi} \tag{4}$$

where $E = |\mathbf{E}|$, $\epsilon(\mathbf{r})$ is the dielectric constant of the dielectric, and the CGS system of units is used. The electric field inside the material can be expressed via an auxiliary potential φ: $\mathbf{E} = \mathbf{E}_0 - \nabla\varphi$, where $\mathbf{E}_0 = (0, 0, E_0)$ is the uniformly applied electric field along the z-axis. We model the dielectric constant by $\epsilon(\mathbf{r}) \approx \bar{\epsilon} + \epsilon_1\psi(\mathbf{r})$, which can be seen as the first two terms of a series expansion of $\epsilon(\psi(\mathbf{r}))$ about $\psi(\mathbf{r}) = 0$. The electric part of chemical potential, eq 4, can be written as $\xi = -\epsilon_1(E_0^2 - 2E_0\nabla_z\varphi + (\nabla\varphi)^2)/8\pi$. It is assumed that $\epsilon_1\psi/\bar{\epsilon} \ll 1$. Therefore, $|\nabla\varphi|/E_0 \ll 1$, and we omit the last term in our treatment. Note that the second term vanishes if $\nabla_z\varphi = 0$. This happens in a structure that is fully aligned with the field direction (the very last stages of alignment process), which is of no interest here. Using the Maxwell equation div $\epsilon\mathbf{E} = 0$, we find in the leading powers of $\nabla\varphi$ and ψ: $\bar{\epsilon}\nabla^2\varphi(\mathbf{r}) = E_0\epsilon_1\nabla_z\psi$. Finally, we arrive at

$$\nabla^2\xi = \frac{E_0^2}{4\pi}\frac{\epsilon_1^2}{\bar{\epsilon}}\nabla_z^2\psi \tag{5}$$

and for the time evolution of the order parameter

$$\dot{\psi} = b\Delta\mu^0 + \alpha\Delta_z\psi + \bar{\eta} \tag{6}$$

where $b = Mv$ is the mobility in the Einstein sense,[41] associated

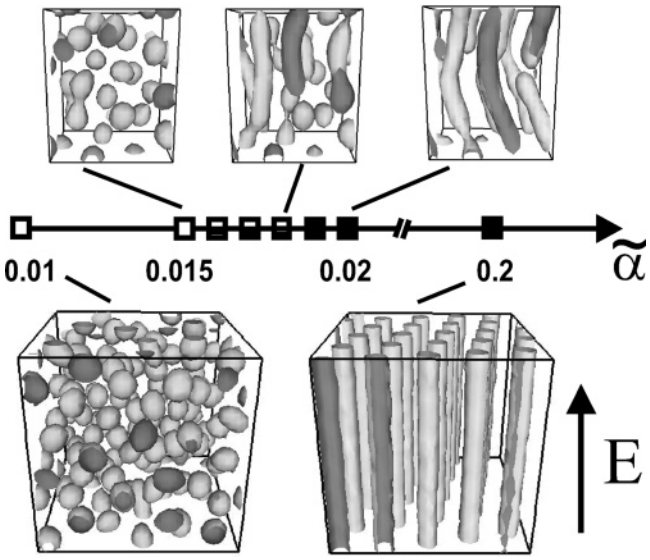

Figure 1. Diagram of structures as a function of the electric field strength $\tilde{\alpha}$ for a bulk $A_3B_{12}A_3$ block copolymer melt with $\epsilon_{AB} = 5.9$ (kJ/mol). The box size is $32 \times 32 \times 32$ grid points (shown completely only for the lower row). The upper rows are details taken from the total simulation volume. All simulations were performed for 6000 time steps in absence of an electric field and consequently 6000 time steps with an electric field. Each square corresponds to one simulation. Structures here and everywhere in the remainder are isodensity surfaces for $f = 0.5$.

with the volume of one polymer chain, $\alpha = bvg_e$, Δ is the Laplacian, $\Delta_z \equiv \partial^2/\partial z^2$, and $\bar{\eta}$ is the properly redefined noise term. The coefficient g_e describes the strength of the electrostatic contribution to the free energy of the system and can be also found in ref 15:

$$g_e = (4\pi\bar{\epsilon})^{-1}\epsilon_1^{\,2}E_0^{\,2}\ (\text{CGS}), \quad g_e = \epsilon_0\bar{\epsilon}^{-1}\epsilon_1^{\,2}E_0^{\,2}\ (\text{SI}) \quad (7)$$

where ϵ_0 is the dielectric constant of vacuum. In the numerical simulations the electric field strength is parametrized by the dimensionless variable

$$\tilde{\alpha} = \frac{\alpha}{kTb} = \frac{\epsilon_0\epsilon_1^{\,2}}{\bar{\epsilon}}\frac{E_0^{\,2}v}{kT}\ (\text{SI}) \quad (8)$$

where $\bar{\epsilon} = \epsilon|_{\psi=0}$ and $\epsilon_1 = \partial\epsilon/\partial\psi|_{\psi=0}$.

The purpose of the present simulation is to determine general features of the kinetic pathway of the transitions and not to search the parameter space for exact values. Nevertheless, it is instructive to estimate whether our parameters are in reasonable experimental reach. We choose the experimental system from our previous study,[27] the most recent detailed experiments for a block copolymer melt available, for which estimates of the electric field strength also have been made in several other theoretical studies.[20,21] We emphasize that the outcome of this exercise only applies to the model system of ref 27. The particular dimensionless values $\tilde{\alpha}$ that we find for the transitions in the systems in the present article (see the section Systems of Interest and the diagrams in Figure 2) should be compared to the actual values in dedicated experiments. Dedicated experiments for our sphere- and cylinder-forming ABA block copolymer melts do not exist at the present moment. However, an estimation along the same lines as below for the system of ref 27, combined with the results of Figure 2, provides a valuable tool for the estimation of the electric field necessary for a transition in future experiments. The experimental system in ref 27 was a PS-*b*-PMMA diblock copolymer melt with

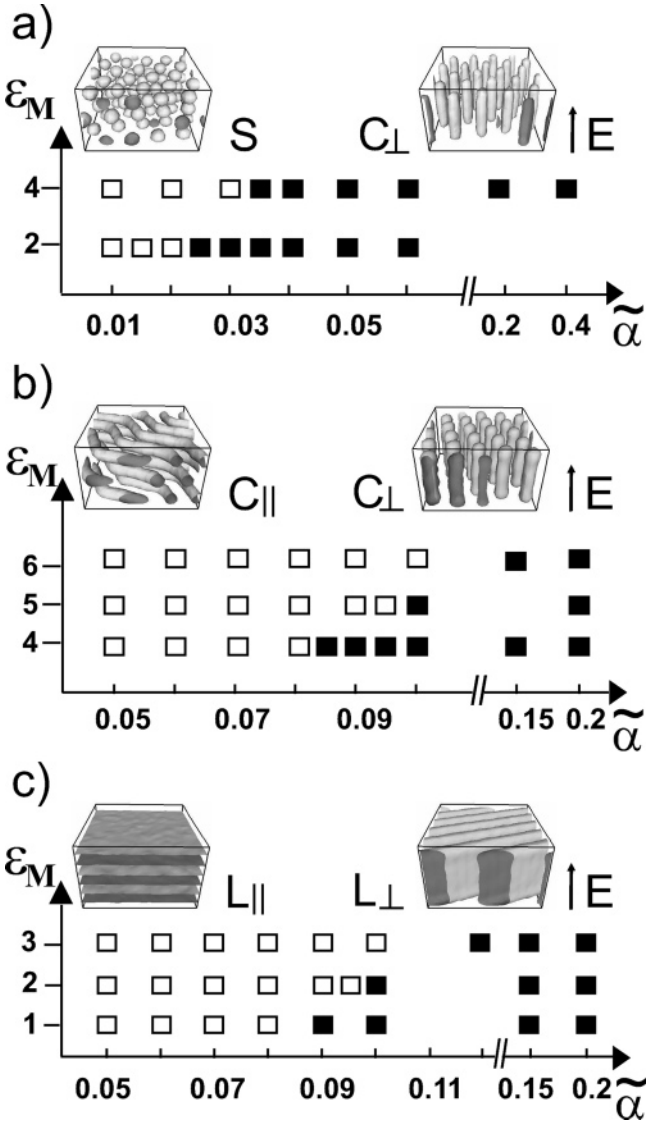

Figure 2. Diagrams of structures in a block copolymer film for varying electric field strength $\tilde{\alpha}$ and surface interaction ϵ_M: (a) spheres $A_3B_{12}A_3$ block copolymer with $\epsilon_{AB} = 5.9$, (b) cylinders $A_3B_{12}A_3$ block copolymer with $\epsilon_{AB} = 6.5$, and (c) lamellae A_4B_4 block copolymer with $\epsilon_{AB} = 7$. Open squares denote parallel structures and full squares perpendicular structures. The box size is $32 \times 32 \times 20$ grid points, with electrodes at $z = 1$, 20. All simulations were performed for 2000 time steps in the absence of an electric field and consequently at least 2500 time steps with an electric field. Here and further, the electrodes at the top and bottom of the simulation box are not displayed.

molecular weight 151K and average PMMA volume fraction $\bar{f} = v\rho^0_{PMMA} = 0.1$. Using the values for the molecular weight of the monomers $M_{PMMA} = 100$ g/mol and $M_{PS} = 104$ g/mol and polymer densities 1.1 g/cm^3 for PMMA and 1.04 g/cm^3 for PS, one finds the volume occupied by one polymer chain equal to $v = 240$ nm^3.[21] We model the dielectric constant by $\epsilon = \epsilon_{PMMA}f + \epsilon_{PS}(1 - f)$ (where $f = v\rho_{PMMA} = \bar{f} + \psi$), which gives $\bar{\epsilon} = \epsilon_{PMMA}\bar{f} + \epsilon_{PS}(1 - \bar{f})$ and $\epsilon_1 = \epsilon_{PMMA} - \epsilon_{PS}$. With respect to the values of the dielectric constants the experimental literature is not very clear. We consider the values for dielectric constants of pure components from refs 20 and 21 $\epsilon_{PMMA} = 6$ and $\epsilon_{PS} = 2.5$, which are the same as the ones stated in ref 27; in ref 42 these constants are given by 5.2 and 3, respectively. In ref 27, we studied two values of the dimensionless $\tilde{\alpha}$: the onset of a sphere-to-cylinder transition (sphere elongation) was observed for $\tilde{\alpha} = 0.1$ and a full transition for $\tilde{\alpha} = 0.5$ (all simulation results in that article were obtained for this value). Using the

expression for the parameter $\tilde{\alpha}$ in SI units, eq 8, we find that for the experimental temperature $T = 170$ °C the electric field is 8 V/μm for $\tilde{\alpha} = 0.1$ and 18 V/μm for $\tilde{\alpha} = 0.5$. The experiments in ref 27 were performed at 40 V/μm. If we alternatively consider the values of earlier work of Amundson,[24] $\epsilon_{PMMA} = 3.8$ and $\epsilon_{PS} = 2.5$, we obtain 20 V/μm (for $\tilde{\alpha} = 0.1$) and 55 V/μm (for $\tilde{\alpha} = 0.5$), which are closer to the experimentally reported electric field.[27] The theoretical work of ref 21 reports a value 79 V/μm as minimal required for sphere-to-cylinder transition at 157 °C. (A calculation for the experimental temperature $T = 170$ °C of ref 27 would result in 80 V/μm and therefore not make much difference.) We conclude that the range of our different estimates for the electric field includes the experimental electric field of Ting et al.[27] All estimates, except one, are somewhat lower than the experimental value. This experimental value was overestimated by the theoretical predictions of Lin et al.[21] The origin of the differences remains a challenge for future work. However, some comments can be made here. (i) A direct comparison with the static calculations in ref 21 is not possible as our structures are often not in equilibrium. In some cases the starting structures (prior to the application of an electric field) are frozen-in metastable states, just like in experimental situations, giving rise to a decrease of the electric field necessary for the transition. In the remainder, this distinction is often highlighted. Moreover, we argue in the results section that this will only affect the electric field necessary for the transition, but not the peculiarities of the transition pathway itself, which are the subject of this study. (ii) Independent investigations of Feng et al.[43] report orientational transitions in lamellar and cylindrical systems under combined (steady shear and electric) external fields for the same range of electric fields as in our study. Their model is a combination of Oono's cell dynamics algorithm and our electrostatic model; their dimensionless electric field parameter (k in ref 43) was taken equal to 0.2. (iii) As discussed in ref 21, a full solution of the Maxwell equation gives a somewhat higher value for the electric field required. This could bring our lower estimates a bit closer to the experimental value. However, we believe that the approximations made in the derivation of our model are well justified in most cases. (iv) As we showed, the estimates are very sensitive to the values of dielectric constants used. The model with dielectric constants of pure components might be not good enough for block copolymer melts. (v) Our model has essentially one free parameter—the physical volume of the problem, which we took as the polymer chain volume. A 2-fold increase of the electric field (from 20 to 40 V/μm), keeping $\tilde{\alpha}$ constant, would lead to a decrease of effective radius of the physical volume by 37%. Physically, this means that the polymer chain configuration is affected by the electric field on a characteristic size comparable with polymer blocks rather than the chain as a whole, and the theory proposed by Gurovich should be reexamined.[13,14]

The dimensionless time step is $\Delta\tau = kTbh^{-2}\Delta t = 0.5$, where h is the numerical grid spacing and the value 0.5 is chosen to ensure stability of the numerical scheme.[36] The Gaussian bond length parameter a, eq 3, and the grid spacing h are related via a so-called grid scaling parameter $ah^{-1} = 1.15$, the value of which is chosen from numerical considerations as well. As b and t enter the simulations only as the product, all simulations can be done in dimensionless time without specifying either of them explicitly. Determining the exact value of the time step is a difficult problem which is out of scope of the present paper. By comparing details of experimentally observed kinetics of phase transition in block copolymers with simulations, we have shown earlier that one simulation time step is about 6 s for the specific system studied.[10] Nevertheless, it is instructive to estimate this value here. Using the notation for the diffusion coefficient $D = kTb$, we get for the time step introduced above $\Delta t = 0.378a^2/D$. We give an estimate for the same system as above.[27] As the majority component (90%) is PS, this block will be the limiting block in the molecular diffusion of the PS−PMMA block copolymer. We take the value for the diffusion of hydrogenated PS (hPS) reported in ref 44 by means of dynamic secondary ion mass spectrometry. For hPS material with molecular weight of 150 K at temperature scaled to 150 °C, the bulk diffusion was found as $D \approx 5 \times 10^{-15}$ cm^2/s. However, as the temperature in ref 27 was 170 °C, the diffusion would be somewhat higher, while, on another hand, the block copolymer molecule diffusivity would decrease due to presence of microphase boundaries. Moreover, there will be a difference in diffusion between hPS and the PS used in ref 27. On top of all this, the diffusion in thin films (the systems of our study) slows down by about 1 order of magnitude as reported in ref 44. The above value is therefore only a rough estimate, which we shall employ in the derivation of the time step. Our model in the work[27] is a Gaussian chain A_2B_{10}, which gives a volume fraction of the A-block equal to $\bar{f} = 0.167$ and chain length $N = 12$. To estimate the Gaussian bond length a, we compare the experimental value for the first-order peak position[27] $q^* \approx 0.174$ nm^{-1} with the analytic expression for $\bar{f} = 0.167$: $q^* \approx 2.19/R$ (where $R^2 = a^2N/6$).[45] Substitution leads to $a \approx 8.9$ nm. Again, this is a rough estimate, as Leibler's expression is not a good approximation for such short chains. Finally, all estimates combined in the expression for the time step give $\Delta t \approx 60$ s, which is well within the experimental range.

We model confined systems by positioning two solid surfaces in the simulation box, representing the electrodes. Both surfaces span the box in the x and y direction completely; in the vicinity of surfaces rigid wall boundary conditions apply.[39] The energetic interactions are fully parametrized by the interaction parameter ϵ^0_{IJ} (bead−bead) and ϵ^0_{IM} (bead−surface), which are the weights of the Gaussian kernels in the expressions for ϵ_{KL} in eq 2 and are given in kJ/mol as in all our previous works.[39] We omit zero superscripts in the following for simplicity. These parameters are directly related to the more familiar Flory−Huggins interaction parameter $\chi = \epsilon/(N_A kT)$, where N_A is Avogadro's number.[36] Although we will operate with ϵ in the remainder of the paper, we will provide the corresponding χN value for all systems under consideration. For the surface interaction in AB and ABA systems the strength is characterized by the value of ϵ_{AM} and ϵ_{BM}. In line with our previous work, we introduce an effective interaction parameter $\epsilon_M = \epsilon_{AM} - \epsilon_{BM}$ since only the difference counts in the calculation of the chemical potential.[46] For all simulations we set $\epsilon_{BM} = 0$. The sign of ϵ_M shows the preferential attraction of A-beads (negative) or B-beads (positive) to the surface.

Minkowski Functionals Method. Modern integral-geometry morphological image analysis provides the tool to assign numbers to the shape and connectivity of patterns formed by pixels of 3-D images, by means of additive image functionals. Examples of such additive image functionals are the Minkowski functionals, which describe the morphological information contained in an image by numbers that are proportional to very simple geometrical and topological quantities: the volume, the surface area, the mean curvature, and the Euler characteristic. Our implementation of the numerical calculation of the Minkowski functionals[47] is adapted from the work of Michielsen et al.[48,49] The Euler characteristic can be understood as the

Table 1. Systems of Study

system no.	chain architecture	ϵ_{AB}, kJ/mol	χN	bulk morphology
1	$A_3B_{12}A_3$	5.8	30.4	S
2	$A_3B_{12}A_3$	5.9	31	S
3	$A_3B_{12}A_3$	6.1	32	C
4	$A_3B_{12}A_3$	6.5	34	C
5	A_4B_4	7.0	16.3	L
6	A_4B_4	8.0	25.7	L

number of connected components minus the number of tunnels (holes) plus the number of cavities. For instance, it is 1 for a solid sphere, 2 for a hollow sphere, 0 for a torus, and -1 for an ∞ shape which has two holes. Because of the additivity, we can use this knowledge for the determination of the topology of the majority part of the local structures from the Euler characteristic. For AB and ABA block copolymers, the amount of amenable mesostructures is limited to spherical, cylindrical, bicontinuous, or lamellar morphologies. This observation leads to a few very simple rules for the interpretation of structures: a very positive Euler characteristic can be interpreted as a majority of spherical or (compact) cylindrical structures and a very negative Euler characteristic as highly connected structures with many tunnels. From the Euler characteristic it is impossible to distinguish between spheres and cylinders of finite length.

III. Objective of the Study

A. Systems of Interest. The same ABA triblock copolymer $A_3B_{12}A_3$ as in our previous studies was chosen to study the electric-field-induced transitions in spherical (S) and cylindrical (C) systems. The behavior of the cylindrical morphologies in confinement was extensively studied for both the symmetric film−surface interactions[9,11] and the asymmetric case;[12] we can use this knowledge to our advantage. Moreover, the bulk diagram of $A_3B_{12}A_3$ was simulated in detail,[11] and we found the following structures as a function of the energetic interaction ϵ_{AB} (in kJ/mol): $\epsilon_{AB} \leq 5.75$, disorder; for $5.8 \leq \epsilon_{AB} \leq 6.0$, A-rich spheres (S); for $6.1 \leq \epsilon_{AB} \leq 6.5$, hexagonally packed A-rich cylinders (C); and for $\epsilon_{AB} \geq 6.6$, A-rich bicontinuous structure (Bic). For electric-field-induced transitions in a lamellar system we have chosen the same symmetric diblock A_4B_4, which was already considered in refs 26 and 28. For this diblock we observe a disordered state in bulk for $\epsilon_{AB} = 6$, while at $\epsilon_{AB} \geq 7$ we observe well-defined lamellar domains. In Table 1 we present a list of chain architecture, ϵ_{AB}, χN, and bulk morphology for the systems studied in this article.

B. Transitions of Interest. In the presence of surfaces (electrodes), microstructures will experience surface effects due to commensurability and surface energetics. For lamellar systems the selective surfaces ($\epsilon_M \neq 0$) induce a parallel orientation and nonselective ($\epsilon_M = 0$) a perpendicular orientation of the lamellae in the vicinity of the electrodes.[8] For cylindrical structures, the same is true albeit that the perpendicular orientations are found at a nonzero ϵ_M value due to a different balance of energetic and entropic contributions to the free energy.[46] For spherical systems, the presence of surfaces leads to the formation of layers of spheres.[50]

In the presence of an electric field, an orientation of microdomains parallel to electric field lines (perpendicular to the electrodes) is energetically favored due to the different dielectric properties of the two blocks. For lamellar and cylindrical systems this effect counteracts the interfacial alignment. In consequence, a minimum electric field strength (threshold electric field strength) is required to overcome the parallel interfacial alignment.[26] Above this threshold, L and C undergo an orientational transition, a $L_{||}$-to-$L_\perp$ and $C_{||}$-to-$C_\perp$ transition, respectively. For spherical systems, the system responds to the applied electric field by elongating in the direction of the electric field, the amplitude of which depends on the strength of the electric field. For spheres the threshold value of interest is the electric field strength at which a S-to-$C_\perp$ transition occurs.

For all film simulations, the electrode surfaces have a preference to the B-block, the strength of which depends on the value of the effective surface interaction parameter ϵ_M. In sphere-forming systems we consider two cases: the thin film system and a bulk system. The phase behavior for a bulk spherical system under an electric field is summarized in Figure 1. The initial structure was obtained after 6000 time steps of simulation without the electric field, starting from homogeneous mixture of components. The spheres are well developed but poorly ordered in space. The simulation time is not sufficient to achieve perfect ordering (see ref 36 for a detailed discussion). We see that a S-to-C transition exists in bulk. The threshold electric field strength for the electric field inducing this transition is around $\tilde{\alpha} = 0.02$. For small values of $\tilde{\alpha}$ the spheres elongate. Upon an increase of the electric field strength, the spheres merge into short cylinders. We found coexisting morphologies of spheres and cylinders (an example is shown as a crop of the simulation box for $\tilde{\alpha} = 0.018$ in Figure 1), where the cylinders are not precisely aligned along the field lines. Even higher values of electric field strength lead to ordered cylindrical domains along the field direction. The same type of transition was observed in refs 20 and 21. The difference with those works is that their transition is abrupt: below the threshold electric field strength there are only elongated spheres and above this value only cylinders. The discrepancy can have several grounds. First, as we emphasized above, our structures are obtained by a simulation method that incorporates dynamics, and therefore they can be metastable. The results of refs 20 and 21 are obtained by static calculations, where all structures are in equilibrium. Moreover, as their calculations are done for Fourier modes, only energies of pure morphologies were compared. Coexisting morphologies are simply no natural subset of the structures considered by their methods.

The phase behavior of block copolymer systems confined in a thin film is presented in Figure 2. Each square represents one simulation. For all thin films no coexisting morphologies were observed in the parameter space studied. For a spherical system confined in a thin film (Figure 2a) all relevant parameters are the same as in system from Figure 1. The threshold depends on the strength of the surface interaction: the stronger the preference of one of the blocks to the surface, the larger the strength of electric field required for the order-to-order transition. Below the threshold value the middle layer of spheres is considerably elongated while layers next to the surface are flattened. We see that the threshold values for the confined system with neutral surfaces (interpolated to $\epsilon_M = 0$) and the bulk system are roughly in the same range ($\tilde{\alpha} \approx 0.02$). The line for $\epsilon_M = 3$ is absent in Figure 2a as for this value of ϵ_M the confinement induces a $C_\perp$ structure in the whole simulation box. For cylinder- and lamellae-forming systems the results are shown in parts b and c of Figure 2, respectively. We see that above the threshold electric field strength all structures swap their orientation. The dependence of this threshold on the surface interaction is approximately linear in both cases.

We note that the diagrams presented here are essentially not *phase diagrams*, as the structures are pathway dependent. In our case, the electric field is applied to an already well-

developed microstructure. Even the situation where in all simulations the electric field is applied from the beginning would not be the same as in the case of the static phase diagram,[19] as the surface-induced microphase separation (initiated by the presence of the electrodes) will play a role as well. This is a fundamental difference between static calculations aimed at deriving equilibrium morphologies and our dynamic simulations. The phase boundaries in our diagrams exhibit hysteresis. The boundaries depend on the history of the sample: the sequence of applying an electric field and the temperature quench. In the following sections we concentrate on the kinetics of the transitions.

IV. Sphere-Forming System

System 1 with $\epsilon_{AB} = 5.8$ ($\chi N = 30.4$) is a spherical system close to the order−disorder transition (ODT) while system 2 with $\epsilon_{AB} = 5.9$ ($\chi N = 31$) is further away from ODT. Although the morphology is spherical, the influence of surface field on the spheres in layers next to the surface can be seen from the fact that these spheres are slightly flattened in the direction parallel to the electrodes. The electrode surfaces have a preference to the B-block.

A. Results. *1. S-to-$C_\perp$ Transition: Far from Disorder.* We start with a spherical system close to the ODT boundary (system 1 in Table 1). The box was chosen to be large enough in both lateral directions to avoid the influence of periodic boundary conditions in these directions. First the system was quenched from a homogeneous melt for 4000 time steps to form a film of three layers of spheres (see Figure 3a, left, time step 4000). At this point an electric field was applied for another 6000 time steps. The final stage after 10 000 time steps is shown in Figure 3a (right). We see that on its way to the final cylindrical state the system passes through the disordered state. The formation of cylindrical structures proceeds via a nucleation and growth mechanism, as there is still a rather large disordered region (gray in Figure 3a) in the middle of simulation box at time step 10 000. A more detailed look at the top view of the system after 4000 time steps (Figure 3a, left) shows equally sized spheres (dots) with grain boundaries between different patches; the inset (detail of the larger box) shows that the structure is indeed spherical in all three layers. The top view of the system after 10 000 time steps (Figure 3a, right) shows thinner dots (indicating perpendicular cylinders, as seen from the inset) with a much better lateral ordering than the initial spheres and fewer grain boundaries. Because of limitation of computational time, we stopped our simulation when the tendency of this transition was clear.

The details of transition are shown in Figure 3b. From this figure we see that the layers next to the electrodes melt almost completely upon application of the electric field while the middle layer melts only partly, leaving a small patch. The $C_\perp$ structure grows from the remaining and partially melted spheres in the middle layer. Several of these seeds (like the one showed in detail in Figure 3b) remain in the full simulation box after melting, being the source of the grain boundaries where the emerging $C_\perp$ clusters meet. The overall structure shows a hexagonal ordering.

2. S-to-$C_\perp$ Transition: Far from Disorder. The second example is a sphere-forming system further away from ODT denoted by one of the squares in Figure 2a (system 2 in Table 1). Figure 4a shows details of the pathway of S-to-$C_\perp$ transition. When the electric field is applied on a microphase-separated melt, the spheres first elongate and become ellipsoidal in shape. Subsequently, the elongated spheres merge to form undulating

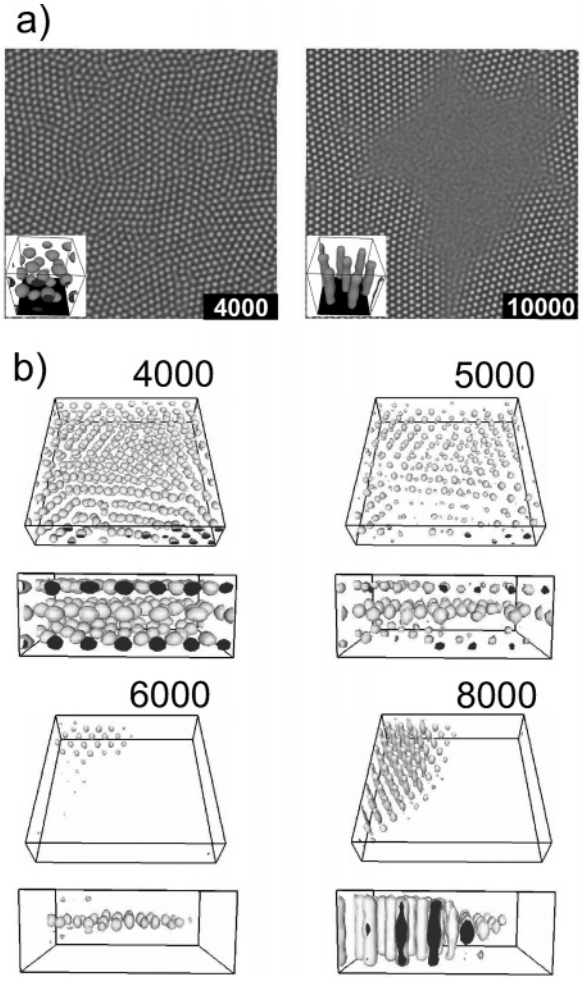

Figure 3. Structural evolution of a $A_3B_{12}A_3$ block copolymer film with $\epsilon_{AB} = 5.8$ and $\epsilon_M = 4$ in a 256 × 256 × 20 simulation box, with electrodes at $z = 1$, 20. (a) Top view of structure at time steps 4000 (at which time an electric field with $\tilde{\alpha} = 0.05$ was applied) and 10 000. Details of simulation boxes are shown as insets. (b) Details of the phase transition dynamics of the system from (a) shown in selected areas of the simulation box: top and side views at corresponding time steps.

cylinders. The interconnections are not oriented in the field direction but, rather, are dictated by the proximity of the ellipsoids. The undulations in the newly formed cylinders decay. Short cylinders rotate as a whole by diffusion. At the end the cylinders are perpendicular to the electrodes (similar to the $C_\perp$ shown top-right in the diagram of Figure 2a and therefore not shown).

Just below the threshold electric field strength the elongation in the direction of the electric field is not sufficient to form perpendicular cylinders. We analyzed the degree of elongation for a constant surface field by plotting the aspect ratio of one sphere as a function of the electric field strength (Figure 4b). The selected sphere is taken from the middle layer where all spheres are equally elongated. We note that no coexistence of spheres and cylinders is observed in any of the confined simulations. The aspect ratio of spheres is approximately linear for the values of $\tilde{\alpha}$ below the threshold. The aspect ratio drops when the S-to-$C_\perp$ transition takes place, indicative of a discontinuous process. The difference with the bulk sphere simulation, where a coexisting morphology is observed (Figure 1), can be attributed to the confinement and the small thickness of the film accommodating three layers of spheres. The abrupt transition seen in Figure 4 is very similar to the one earlier reported by static calculations in ref 20 (compare their Figure 1; see also the discussion of our Figure 1).

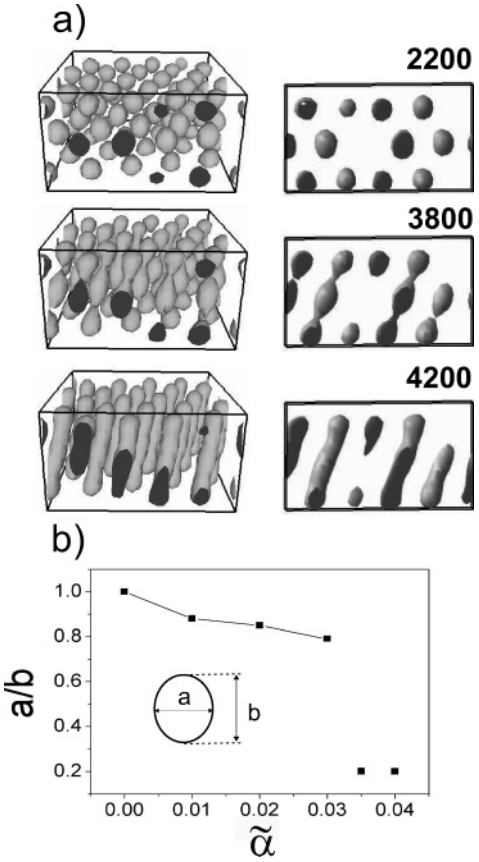

Figure 4. (a) Structural evolution of a $A_3B_{12}A_3$ block copolymer film with $\epsilon_{AB} = 5.9$ and $\epsilon_M = 4$ in a $32 \times 32 \times 20$ box, with electrodes at $z = 1$, 20. An electric field ($\tilde{\alpha} = 0.04$) was applied after an initial 2000 time steps. The right column shows side views at corresponding time steps. (b) Aspect ratio of a sphere as a function of electric field strength. The spheres were taken from the middle layer of the simulation box. The cylinder length b for $\tilde{\alpha} = 0.035$, 0.04 is finite due to confinement.

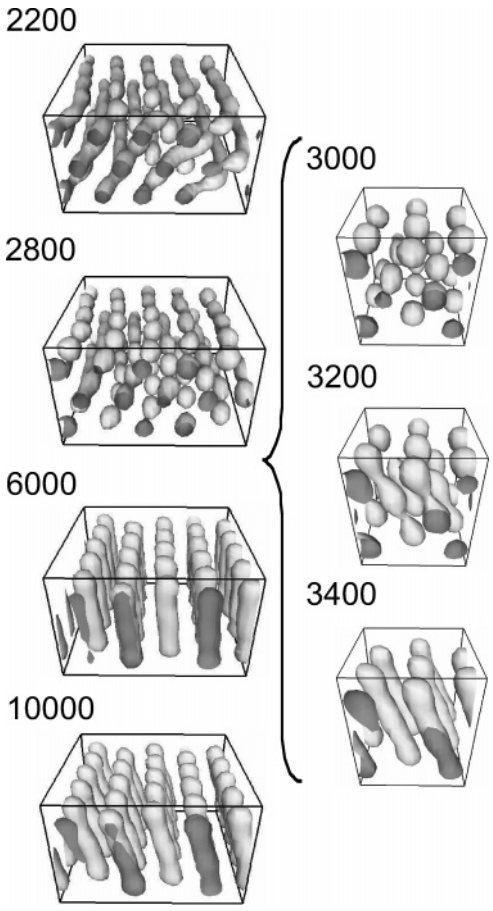

Figure 5. Structural evolution of a $A_3B_{12}A_3$ block copolymer film with $\epsilon_{AB} = 6.1$ and $\epsilon_M = 4$ in a $32 \times 32 \times 20$ box, with electrodes at $z = 1$, 20. The electric field ($\tilde{\alpha} = 0.06$) was applied between 2000 and 6000 time steps. Structures between 3000 and 3400 time steps are shown as parts of the total simulation box (right column).

B. Discussion of the Kinetic Pathways of S-to-$C_\perp$ Transition. When a system is close to ODT (system 1 in Table 1), the S-to-$C_\perp$ transition proceeds via partial melting into the disordered phase in thin film, as illustrated in Figure 3. In the vicinity of surfaces there are two opposite tendencies: the surface field tends to elongate spheres along the surface, and the electric field tends to elongate spheres along the field lines. Close to ODT, this competition leads to partial disordering (melting) of the system. For the thin film the remaining or partially melted spheres in the middle layer serve as a nucleus for a new $C_\perp$ phase. The overall mechanism can be characterized as a nucleation and growth mechanism. As the surface field is of short range,[9,46] its influence on the microstructure is the strongest in the vicinity of electrodes. This explains why we observe melting in the layers next to the surfaces. To verify this statement, we performed a simulation for a twice thicker film and smaller lateral dimensions ($32 \times 32 \times 40$, results not shown here). After application of the electric field the layers next to the surface melt while spheres in the middle of the film elongate and connect into perpendicular cylinders. No melting was observed in the middle of the film.

In a system further away from ODT (system 2 from Table 1, illustrated by Figures 2a and 4), the competition of surface field and electric field does not lead to melting, but to the elongation of spheres in the direction of the electric field; the shape depends on the balance between the ponderomotive force and surface tension.

Experimentally, the electric-field-induced sphere-to-cylinder transition in thin films was observed in detail for a diblock system.[27] In ref 27 a direct comparison of our method with experimental TEM and AFM snapshots for a diblock copolymer melt and one value of block−block interaction showed a 1−1 correspondence of the transition pathway, including the coexistence of spheres and cylinders during the merging process. Here we show that these details are also observed for an ABA triblock. We conclude that the transition pathway is most sensitive to the degree of microphase separation, and rather independent of the polymer architecture.

V. Cylinder-Forming System

In the phase diagram, the cylinder-forming system is surrounded by the spherical (lower χN) and the bicontinuous (higher χN) phase. System 3 from Table 1 with $\epsilon_{AB} = 6.1$ ($\chi N = 32$) is close to the phase boundary with the spherical phase while system 4 with $\epsilon_{AB} = 6.5$ ($\chi N = 34$) is close to the boundary with bicontinuous phase.

All simulations were performed in a simulation box that accommodates three parallel layers of cylinders. The electrodes have an energetic preference to the B-block.

A. Results. *1. $C_{||}$-to-$C_\perp$ Transition: Close to Spheres.* For system 3 the electric field was applied between 2000 and 6000 time steps only. The transition kinetics is shown in detail in Figure 5. The starting structure is three layers of parallel cylinders at 2000 time steps. Upon application of an electric field the parallel cylinders start to undulate with a wavelength

roughly equal to the distance between the cylinders (time step 2200). At the next stage the system breaks up into well-distinguished spheres in the whole box (time step 2800). Upon comparing the time evolution of the sphere-forming system from Figure 4 (time steps 2200−4200) and the cylinder-forming system from Figure 5 (time steps 3000−3400), we see that the next stages in the $C_{||}$-to-$C_{\perp}$ transition follows exactly the same route as the S-to-$C_{\perp}$ transition (section IV.A.2).

The detailed snapshots in Figure 5 (right) show that the spheres merge with each other to form undulating cylinders in a tilted direction with respect to the direction of the electric field (time step 3400); the origin is similar to described in section IV.A.2. At the end the cylinders are perpendicular to the electrodes (time step 6000).

To ensure that the final cylinders are not a kinetically driven metastable phase in the region of the phase diagram where spheres are the actual stable equilibrium structure, we have continued our simulation with the electric field switched off for another 4000 time steps to see if they eventually break up into spheres. Figure 5 (time step 10 000) shows that the structure remains cylindrical but experiences a slight tilt with respect to the direction perpendicular to the electrodes. We attribute this tilt to the interplay of energetic and entropic factors associated with the surfaces. The surface prefers the B-blocks; the A-rich cylinder caps close to the surface represent an energy penalty. In a search for the least frustrated situation the system finds a slightly tilted orientation. In the presence of an electric field this tilt is suppressed by the tendency of the system to avoid dielectric interfaces under an angle to the field lines.

2. $C_{||}$-to-$C_{\perp}$ Transition: Close to Bicontinuous. Next we focus on a system 4 from Table 1. We compare two systems with the same χN but different defect density. We consider systems at different positions in the diagram in Figure 2b, as it is not easy to find a system without long-lasting defects due to the relatively low energy cost of these defects. The system in Figure 6a has no defects in the initial structure prior to applying an electric field, while that in Figure 6b has a defect in the form of an open end of a cylinder before the electric field was applied. In both cases the electric field is close to the threshold electric field strength.

In the system without defects (Figure 6a) the transition goes via undulation instabilities, leading to a breakup of the system in the whole box almost instantly. The system with a defect (Figure 6b) follows a defect-mediated transition: the open end of the cylinder serves as a nucleus for the formation of the new $C_{\perp}$ phase.

We provide additional insight on the pathway of the defect-free system by considering the top view of the structure (right column in Figure 6a). It confirms that the transition takes place via undulations with primary wavelength roughly equal to the distance between the cylinders and that the breakup takes place in whole box almost simultaneously. The cylinders not only undulate in shape but also at larger scale adapt their position and curvature in space. The latter leads to a complete re-arrangement of the undulations into a hexagonal lattice even before the cylinders actually break and reconnect to form the new perpendicular cylinders.

The transition times in Figure 6a (undulation and breakup at once) and Figure 6b (defect-mediated) cannot be directly compared to each other due to the difference in both electric field strengths and surface interactions. Figure 7 shows the free energy without electrostatic contribution for a range of electric field strengths (black squares in Figure 2b) and constant effective interaction with surface. We have chosen to consider the free

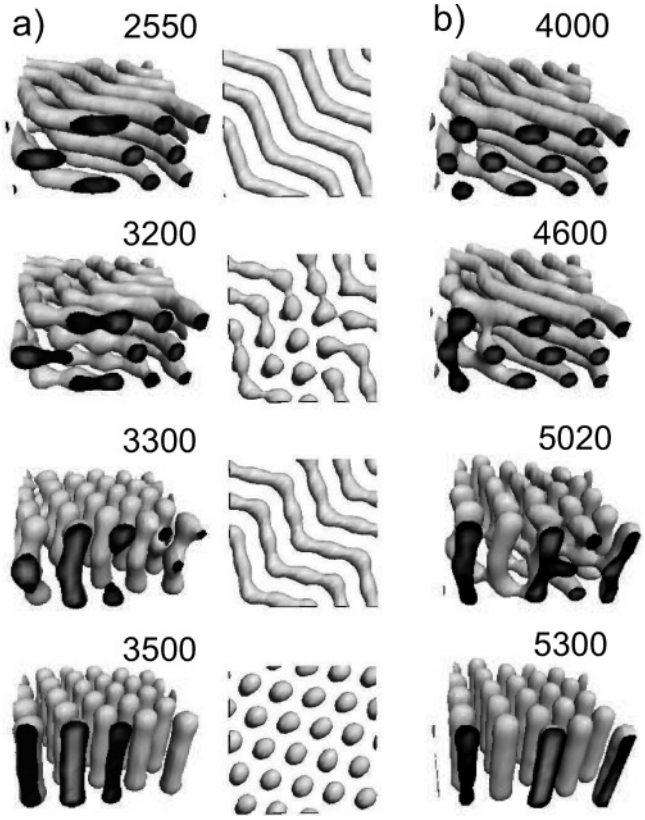

Figure 6. Structural evolution of a $A_3B_{12}A_3$ block copolymer film with $\epsilon_{AB} = 6.5$ in a $32 \times 32 \times 20$ box, with electrodes at $z = 1$, 20. The electric field was applied after an initial 2000 time steps. (a) $\epsilon_M = 6$ and $\tilde{\alpha} = 0.15$; left, side view; right, top view. (b) $\epsilon_M = 4$ and $\tilde{\alpha} = 0.082$.

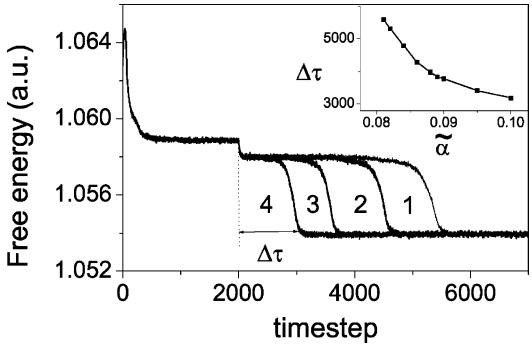

Figure 7. Time evolution of free energies without the electrostatic contribution for simulated systems from Figure 2b with $\epsilon_M = 4$ and varying electric field strengths $\tilde{\alpha} = 0.082$ (1), 0.084 (2), 0.086 (3) and 0.088 (4), respectively. The electric field was applied at 2000 time steps. The orientation transition time $\Delta\tau$ as a function of electric field strength $\tilde{\alpha}$ is shown as an inset.

energy without electrostatic contribution, as this reduced free energy will provide us insight into the change of the degree of microphase separation in time and changes in shapes of the cylinders, like undulations. The simulation, of course, has accounted for the total free energy, as described in section II.

In all cases, at 2000 time steps the electric field was applied which is seen in the graphs as a small jump down, after which the systems reaches a plateau. This plateau corresponds to undulated cylinders (see Figure 6a,b). One may consider the plateau as an excited state with a lifetime that depends on the strength of the applied electric field. Consequently, the length of the plateau is an indication of the characteristic lifetime of this exited state. This length (in time steps) is plotted as an inset in Figure 7 as a function of electric field parameter. It

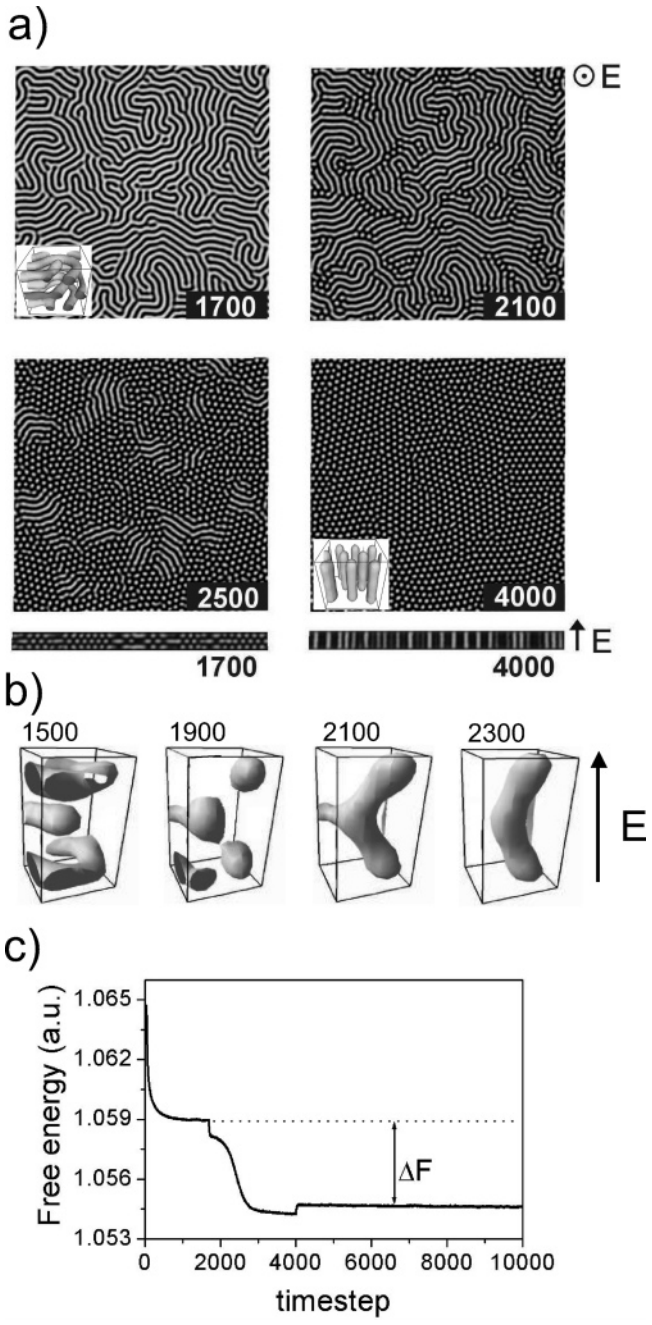

Figure 8. Structural evolution of a $A_3B_{12}A_3$ block copolymer film with $\epsilon_{AB} = 6.5$ and $\epsilon_M = 4$ in a $256 \times 256 \times 20$ box, with electrodes at $z = 1$, 20. The electric field ($\tilde{\alpha} = 0.1$) was applied between 1700 and 4000 time steps. (a) Top view at 1700, 2100, 2500, and 4000 time steps and side view at 1700 and 4000 time steps. Details of the total simulation box are shown as insets. (b) Time evolution of a single defect in the system from (a) shown via selected regions of the total simulation box.

decays as a function of the electric field strength. Cylinders break up and the recombination is fast: after the plateau, the free energy without the electric field contribution decreases quite rapidly to the value that corresponds to a perpendicular orientation of cylinders.

The defect-mediated transition can be seen most clearly in a laterally larger box (see Figure 8). For this simulation we took one of the systems from the diagram in Figure 2b. In the absence of an electric field, the system forms three layers of parallel cylinders with many typical defects like open ends of cylinders (time step 1700). After the electric field was applied, nuclei of the $C_\perp$ phase form at the position of defects in the structure. At their edges the newly formed perpendicular clusters grow in the lateral direction leading to the formation of several grains of hexagonally packed cylinders perpendicular to the electrodes. The electric field cannot help in eliminating the grain boundaries, as the free energy of the hexagonal pattern is invariant with respect to rotation around the cylinder axis (the electric field direction).

Figure 8b shows the details of the transition kinetics, focusing on a nucleus of the $C_\perp$ phase still surrounded by $C_{||}$. The open end of a cylinder initiates the appearance of open ends in the neighboring layers. Consequently, the open ends swell and eventually connect with each other in a characteristic three-arm connection. Because of these connections between neighboring cylinder layers, the system becomes bicontinuous: a three-arm connection is characteristic for the gyroid phase. We observe rows of such three-arm connections forming a front. This front propagates inside the $C_{||}$ phase, thus forming a cluster of perpendicular cylinders. Figure 8b shows that the three-arm connections break and transform into banana-shape cylinders, which slowly straighten. A whole box of these banana-shape cylinders can be already seen in Figure 6a (time steps = 3300), suggesting that newly formed cylinders are never perfectly aligned in the direction of the electric field.

We now focus on the remark about metastability (comparison to the equilibrium theory of Lin et al.;[21] remark i in the Model section) and illustrate our repeated notion that the diagrams in Figure 2 are essentially *no* phase diagrams. Earlier in ref 11 we calculated a diagram for varying surface energetics ϵ_M and thickness H for the same $A_3B_{12}A_3$ triblock copolymers ($\epsilon_{AB} = 6.5$) in the absence of an electric field (Figure 8 in that article). From this diagram we observe that the systems of Figures 6b and 8a ($\epsilon_M = 4$ and $H = 18$) are within the $C_{||}$ region, but close to the boundary with $C_\perp$, while the system of Figure 6a ($\epsilon_M = 6$ and $H = 18$) is much deeper into the $C_{||}$ region. If we now concentrate on the large system of Figure 8a ($\epsilon_M = 4$) and switch the electric field off after all cylinders have reoriented themselves into perpendicular ones (time step 4000), we observe that they remain in this perpendicular orientation and do not transform back to the parallel orientation. We can rationalize this observation by considering in Figure 8c the free energy without electrostatic contribution of the system from Figure 8a. After 4000 time steps the electric field was switched off. In the absence of the electric field, i.e., before 1700 time steps and after 4000 time steps, the free energy shown in Figure 8c is the total free energy of the system, and it is lower for the perpendicular cylinders. We conclude that the starting configuration of parallel cylinders was a kinetically trapped state caused by the surface-induced phase separation. Without external help, like the electric field in this case, the system will never change its orientation, as the thermal fluctuations are too small to overcome the energetic barrier imposed by the presence of selective surfaces preferring the parallel orientation. This is the fundamental reason for the previously mentioned "hysteresis", meaning that the location of phase boundaries depends on the kinetic history of the system.

In Figure 9 we show large-scale simulation snapshots of the structural evolution of an initially homogeneously mixed confined system for a much stronger surface field ($\epsilon_M = 7$ and $H = 18$). A twice stronger electric field was applied between time steps 1700 and 4000 in order to induce an orientational transition (see Figure 2). In the diagram of Figure 8 in ref 11, this system is located toward the center of the $C_{||}$ region and relatively close to the surface-field-induced perforated lamellae (PL) region. In the absence of an electric field the system forms

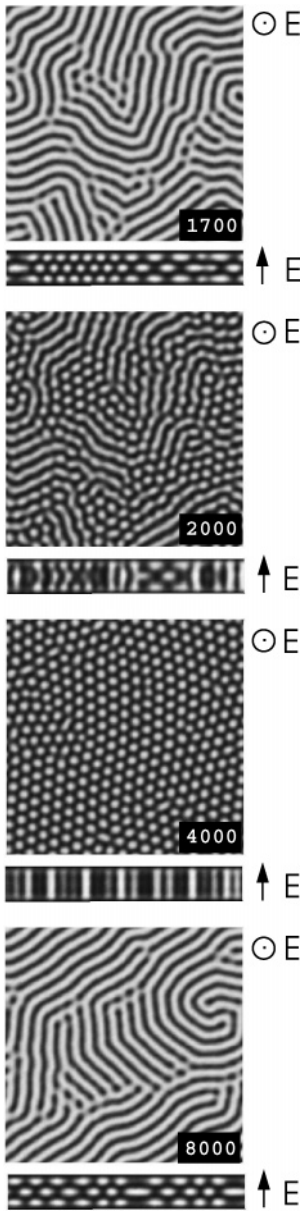

Figure 9. Structural evolution of a $A_3B_{12}A_3$ block copolymer film with $\epsilon_{AB} = 6.5$ and $\epsilon_M = 7$ in a $128 \times 128 \times 20$ box, with electrodes at $z = 1$, 20. The electric field ($\tilde{\alpha} = 0.2$) was applied between 1700 and 4000 time steps. From top to bottom: top and side views at 1700, 2000, 4000, and 8000 time steps.

three layers of parallel cylinders with typical ringlike defects (Figure 9, time step 1700). After the electric field was switched on at time step 1700, these defects serve as nuclei of the new $C_\perp$ phase (Figure 9, time step 2000), just like in the system of Figure 8a. The main difference between these two systems is that these defects are now ringlike (patches of the neighboring PL phase) instead of cylinder ends. These newly formed perpendicular clusters grow in the lateral direction, leading to the formation of several grains of hexagonally packed cylinders perpendicular to the electrodes (Figure 9, time step 4000). The details of the transition are very much alike the ones illustrated by Figure 8b and therefore not shown. However, because of the stronger electric field, the process is much faster. In contrast to the system of Figure 8, the perpendicular cylinders in Figure 9 transform back into parallel cylinders after switching the electric field off at time step 4000. This back-transition from $C_\perp$ to $C_{||}$ takes place via bicontinuous intermediates, just like the initial $C_{||}$ to $C_\perp$ orientational transition under the influence

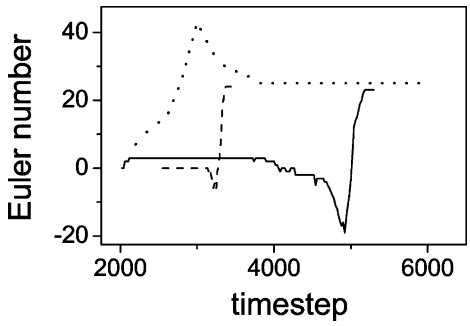

Figure 10. Time evolution of the Euler characteristics in cylinder-forming systems: the system from Figure 5 (dotted line), the system from Figure 6a (dashed line), and the system from Figure 6b (solid line).

of the electric field. At the end of this back-transition the free energy levels off to a constant value that is comparable to the free energy level before the electric field was switched on (time step 1700), indicative of a $C_{||}$ structure being the most stable structure for this system. The final stage at time step 8000 in Figure 9 shows three layers of parallel cylinders, again with ringlike defects. The situation before and after the electric field was switched on is roughly comparable in terms of defect density; the position of the defects is clearly different.

B. Discussion of Kinetic Pathways of $C_{||}$-to-$C_\perp$ Transition. We have considered two types of cylinder-forming systems with different degree of microphase separation depending on which the system undergoes the $C_{||}$-to-$C_\perp$ transition via different pathways. The $C_{||}$-to-$C_\perp$ transition via an intermediate S phase was found experimentally.[51] We will confirm our earlier statements more quantitatively using the evolution of the Euler characteristics.[47]

As an example of a cylinder-forming system with lower degree of microphase separation (system 3 in Table 1), we considered the system from Figure 5. From visual inspection it is clear that spheres are an intermediate structure for the $C_{||}$-to-$C_\perp$ transition in this system. As an example of a cylinder forming system with higher degree of microphase separation (system 4 in Table 1) we considered two systems from Figure 6a,b. Visual inspection of images suggests that the intermediate structure in the $C_{||}$-to-$C_\perp$ transition for defected and defect-free structures is a bicontinuous one. The temporal Euler characteristic plots in Figure 10 provide additional information. While the initial and final values are similar for all systems, the intermediate region for system 3 (dotted line) is highly positive, corresponding to spheres. Both graphs for systems 4 (dashed and solid) start from the value close to 0, which corresponds to parallel cylinders seen as tori (with Euler characteristic equal to 0) due to periodic boundary conditions in the lateral directions. The solid line for the system shown in Figure 6b has a positive starting value due to the broken cylinder which is topologically seen as a sphere (Euler characteristic equal to 1). With time both graphs drop to negative values, corresponding to an interconnected structure. In the defect-free case this intermediate state is very short living. At the final stage both graphs take a positive value, corresponding to perpendicular cylinders, which are topologically seen as spheres due to the presence of the electrodes. As a matter of fact, the Euler characteristic at the final stages is equal to the total number of perpendicular cylinders (as the Euler characteristic for a single cylinder is equal to 1).

In all observed transitions in cylinder-forming systems undulation instability plays an important role. In the $C_{||}-C_\perp$ transition for lower degree of microphase separation the

undulations enable the system to break up to spheres (see Figure 5). The growth of undulation instability enables the $C_{||}$-to-$C_{\perp}$ transition in a defect-free structure as well (see Figure 6a,c). Undulation instability also plays a role in the defect mediated transition (see Figures 6b, 8a,b, and 9). In such systems undulations are particularly important for the formation of nuclei of the $C_{\perp}$ phase at the location of defects in the parallel microstructure. This finding is in agreement with an earlier suggested mechanism[32] where transitions in cylinder-forming thin film was enabled by a developing undulation instability, leading to the disruption of an oriented domain and followed by reorientation or rotation of small grains.

VI. Lamellae-Forming System

We showed earlier for 2D system[26,28] that nucleation (via undulations and local structure breakage) and growth is the governing mechanism for lamellar systems with lower degree of microphase separation, while rotation of grains (via movement of defects and annihilation of opposite sign defects) is the main mechanism for lamellar systems with a high degree of microphase separation. Here, we focus on the detailed kinetics of these orientational transitions in three dimensions. We have chosen a diblock A_4B_4 melt, the same as used in our previous studies in 2D.[28]

A. Results. *1. $L_{||}$-to-$L_{\perp}$ Transition: Close to Disorder.* Figure 11a shows the details of the dynamics of the transition from lamellae parallel to the electrodes ($L_{||}$) to lamellae perpendicular to the electrodes ($L_{\perp}$) for system 5 (Table 1), corresponding to one of the squares in Figure 2c. We observe lamellar undulations appear after the electric field was applied. The wavelength of the undulations is roughly equal to the interlamellar spacing, which can be seen from the 2D slices (side view, right column in Figure 11a, 2200 and 2300 time steps). Undulated lamellae evolve into a highly connected bicontinuous structure (time step 2300). This intermediate structure quickly changes to a $L_{\perp}$ structure (time step 2600) with some remaining defects. The defects in the $L_{\perp}$ are persistent even after a long time: only a small defect rearrangement is visible between 2600 time steps and 8000 time steps. At stronger electric fields defect-free structures are easily obtained (similar to the right snapshot in Figure 2c). Our intermediate stage of undulated lamellae is visually similar to the morphology found in static calculations in ref 19 as a superposition of $L_{||}$ and $L_{\perp}$ close to the threshold electric field strength (compare their Figure 4b and our Figure 11a at 2200 and 2300 time steps). The nature of the intermediate stage of the $L_{||}$-to-$L_{\perp}$ transition in Figure 11a is clarified by the time evolution of Euler characteristics presented in Figure 11b. The zero Euler characteristic value at time step 2000 corresponds to perfect lamellae. After the electric field is applied the Euler characteristic rapidly drops to very negative values, corresponding to a highly interconnected (bicontinuous) structure. At the final stage the Euler characteristic has a small negative value reflecting the presence of long-living defects in the final $L_{\perp}$ structure (see Figure 11a, time step 8000).

The left column in Figure 11c shows details of $L_{||}$-to-$L_{\perp}$ transition by means of horizontal slices through the lamellae shown in Figure 11a. Initially, the density of A-component is homogeneous, corresponding to well-microphase-separated lamellae, parallel to the *xy* plane. After the electric field is switched on, several brighter and darker patches appear. These patches reflect the undulations in the lamellae. The regions of perpendicular structures that are formed when time progresses rearrange themselves quickly into parallel stripes. It is remarkable that the whole process of orientational phase transition as seen

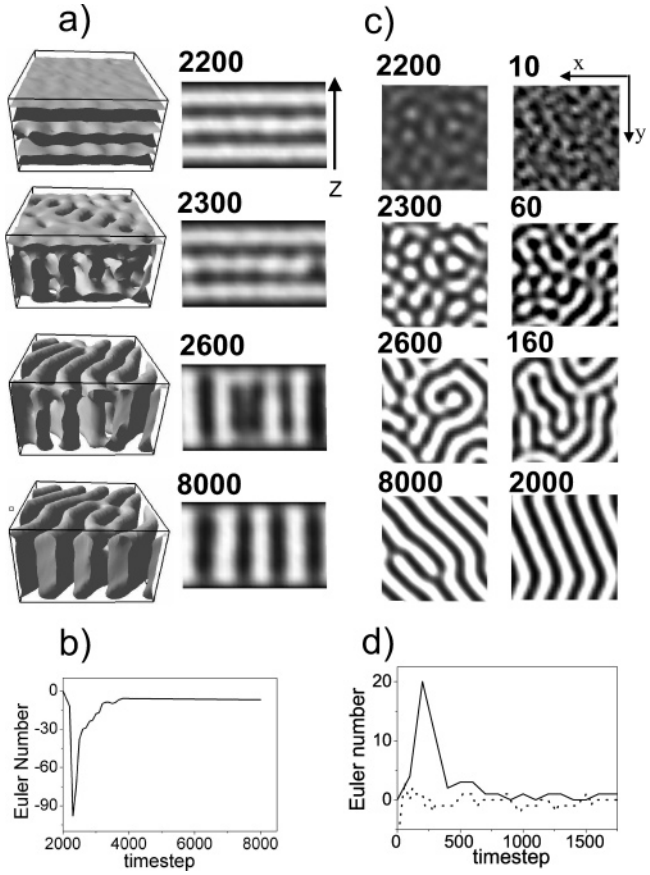

Figure 11. (a) Structural evolution of a A_4B_4 block copolymer film with $\epsilon_{AB} = 7$ and $\epsilon_M = 3$ in a $32 \times 32 \times 20$ box, with electrodes at $z = 1$, 20. The electric field ($\tilde{\alpha} = 0.12$) was applied at 2000 time steps. (a) Left, 3D views; right, side view on a vertical slice. (b) Time evolution of Euler characteristic for the system from (a). (c) Left, horizontal slices ($z = 6$) at different time steps for the system shown in (a); right, structural evolution of the same block copolymer in a 2D box (32×32), in the absence of an electric field. (d) Time evolution of the Euler characteristic for the systems shown in (c): solid line, left column; dashed line, right column. To enable a comparison, we shifted the starting time for the system in the right column of (c) by 2000 time steps.

in the 2D slices is visually similar to a microphase separation of a 2D lamellar system following a temperature quench in the absence of an electric field (Figure 11c, left). Starting from a homogeneous mixture, fluctuations lead to the formation of spheres, followed by their merging into compact elongated structures, and finally to the formation of lamellar stripes. The naive conclusion would be that the paths through the energy landscapes of these two phenomena are similar, although they are very different in nature.

To challenge the presumed similarity from this visual inspection, we compare the evolution of the Euler characteristic for both simulations in Figure 11d. From this comparison we see that the behavior is quite different: the 2D slices of the 3D system (solid line) have a rather positive Euler characteristic in the initial stages, indicating many disconnected structures. The system from right column of Figure 11c is somewhat negative, indicating an interconnected, bicontinuous structure. From this comparison, we see that it can be dangerous to compare different systems on the basis of visual inspection alone.

2. $L_{||}$-to-$L_{\perp}$: Far from Disorder. Finally we consider system 6 (Figure 12), which is the 3D analogue of the 2D system in our earlier simulation study[28] and the associated experimental/simulation work.[26] In the simulations in these works confinement was absent (we considered structures in the bulk) while here

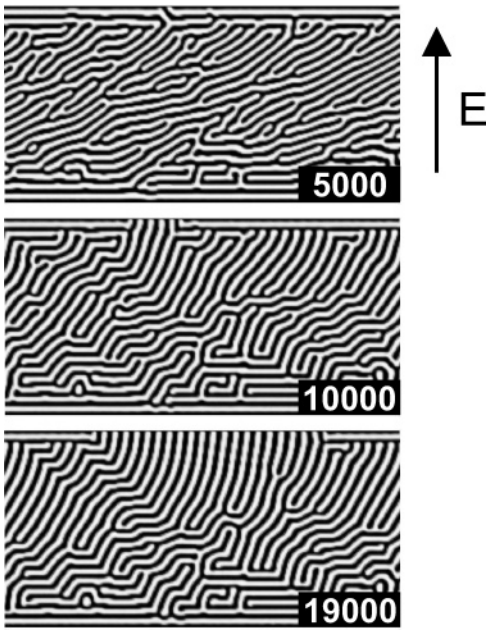

Figure 12. Structural evolution of a A_4B_4 block copolymer film with $\epsilon_{AB} = 8$ and $\epsilon_M = 2$ in a $256 \times 4 \times 128$ box, with electrodes at $z = 1, 128$. An electric field ($\tilde{\alpha} = 0.2$) was applied at 5000 time steps after an initial 2500 time steps of microphase separation and an additional 2500 time steps of preshearing. The structures are shown on vertical slices parallel to the *xz* plane.

electrodes are present at the top and bottom of the sample and have a preferential attraction to one of the blocks. The interaction with the electrodes is relatively short ranged. The small *y*-dimension of the simulation box allows us to keep the computational effort within limits while it still gives additional freedom to the lamellae. We do not expect much to happen in this direction, and therefore we choose to keep only the other two dimensions as large as possible. This practice is accepted in large-scale simulations, when one of the dimensions is considered not to be of crucial importance.[52]

First the system was quenched for 2500 time steps, after which it was presheared for another 2500 time steps (total shear strain was 250%). The role of the preshearing is to create a sample with reasonable uniform alignment but still with a high defect density.[28] At 5000 time steps, the electric field was applied. In Figure 12 we observe that rotation by defect movement is the dominant mechanism of realignment, similar to the mechanism observed for this system in 2D.[28] In the middle of the film lamellae orient in the electric field direction, while close to the substrates, regions of predominantly parallel orientation remain. At the positions where perpendicular and parallel lamellae meet, a connection in the shape of a T-junction is formed. This structure is very similar to the mixed morphology in static calculations[19] (their Figure 5). In experiments with much thicker films of polymer solutions and relatively strong polymer−electrode energetic interaction, a mixed morphology was also found to be persistent.[53] The final structure at 19 000 time steps is highly defected but shows a clear tendency for lamellae to align in the electric field direction. During this transition, the system remains lamellar. No intermediate structures with other symmetries have been observed.

B. Discussion of Kinetic Pathways of $L_{||}$-to-$L_{\perp}$ Transition. For systems with a weak A/B interface the $L_{||}$-to-$L_{\perp}$ transition takes place via a bypass in the neighboring bicontinuous phase. We do not observe any significant melting of the structure into a disordered state. Therefore, the present pathway is not trivial to guess. The naive suggestion would be that the application of an electric field just shifts the system along the temperature axis in phase space. This would lead to (partial) melting and consequent buildup of new lamellae from disorder, as the symmetric block copolymer melt can only form lamellar or disordered phases. Our results suggest that the pathway in phase space is much more elaborated. The system develops undulation instability. It was already shown by Onuki and Fukuda[15] that this process can happen in a certain range of the parameters controlling the lamellar interfacial strength and the electric field value. Such interfaces are considered to be weak (this term should not be mixed up with weak segregation, which is indifferent to the presence or absence of an electric field). Another important conclusion from our results is that the new $L_{\perp}$ phase emerges immediately from the intermediate bicontinuous phase. Therefore, the system can in principle have clusters of only two lamellar orientations: decaying $L_{||}$ and growing $L_{\perp}$. Although we do not perform very large-scale simulations here, our earlier 2D study in very large simulation boxes supports this conclusion.[28] As we showed in ref 28, the new $L_{\perp}$ phase appears via nucleation at the position of defects. It was shown in refs 26 and 28 that nucleation and growth is the main mechanism in the orientational transition in lamellar systems with low degree of microphase separation.

For the systems with stronger A/B interface (higher χN parameter) the transition follows another pathway. During the whole transition, the system remains completely in the lamellar phase. Because of a stronger interfacial tension, undulation instability will not grow for electric field strengths sufficient to initiate undulations in systems with weaker interfaces. The presence of defects is therefore a prerequisite in this transition. Typical defects are open ends of lamellae. Under the influence of an electric field, defects propagate perpendicular to the lamellar stripes. Defects of different sign propagate in opposite direction and occasionally annihilate when two of them meet. This leads to local rotation of a small piece of lamellae. The process continues until all defects are gone.

VII. Conclusions

We studied the behavior of confined systems of sphere-, cylinder-, and lamellae-forming block copolymers under an applied electric field by means of dynamic self-consistent theory. We summarize our results here.

Threshold Value of Electric Field Strength. When no electric field is applied, the majority of cylinder- and lamellae-forming systems experiences alignment parallel to the electrodes. In sphere-forming systems, the presence of electrodes leads to the formation of layers of spheres. When a sufficiently strong electric field is applied, the orientation of microdomains switches to perpendicular to the electrodes (parallel to external electric field lines). Sphere-forming systems respond to the applied electric field by elongating spheres in the direction of the electric field, the amplitude of which depends on the strength of the electric field. Lamellar- and cylinder-forming systems undergo an orientational transition while spheres undergo a phase transition with a change of symmetry.

The threshold value of the electric field strength $\tilde{\alpha}$ (quadratic in E_0) is found to be approximately linear in the effective surface interaction parameter ϵ_M. For spheres surface energetics modifies the behavior similar to the cylindrical and lamellar case.

Kinetic Pathways of Phase Transitions. The major take-home message of this paper is that the kinetic pathway taken by a system near a phase transition can be very different from one that is far from a phase transition (illustrated by Figure 13).

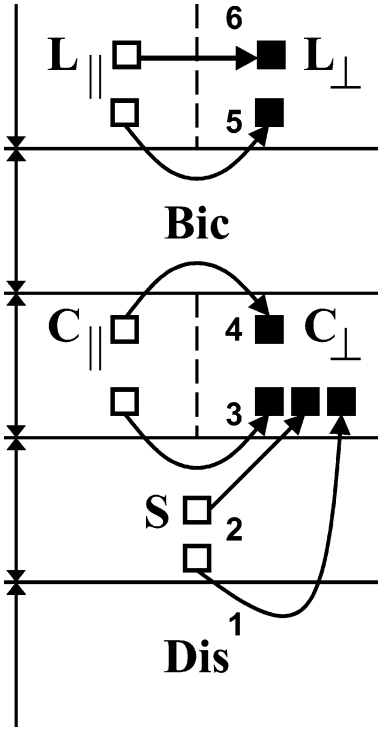

Figure 13. Schematic diagram summarizing kinetic pathways (denoted by arrows) for sphere (S)-, cylinder (C)-, and lamellae (L)-forming systems under an electric field. Open squares denote initial positions; black squares denote positions after the phase transition."Dis" denotes disordered phase and "Bic" a bicontinuous phase.

Sphere-forming systems close to ODT undergo a sphere-to-cylinder transition with partial disordering of a system in a transient state (schematically shown as pathway 1 in Figure 13). Sphere-forming systems further away from ODT transform into cylinders via elongation and merging of spheres (pathway 2 in Figure 13). Cylinder-forming systems close to the boundary with spheres transform into the spherical phase on their way to the $C_{\perp}$ structure (pathway 3 in Figure 13). Cylinder-forming systems close to the boundary with the bicontinuous phase transform via an intermediate bicontinuous structure (pathway 4 in Figure 13). In a lamellae-forming system we found two distinctly different mechanisms for the $L_{||}$-to-$L_{\perp}$ transition. In a system relatively close to the ODT the transition goes via a transient bicontinuous phase (pathway 5 in Figure 13). The transition via a local rotation of lamellar grains caused by defect movement was observed in a system further away from ODT (pathway 6 in Figure 13). The system remains in the lamellar phase during the whole transition.

Defects and Undulations. Structural defects and undulation instability play an important role in the phase transition under an electric field, and the associated mechanisms depend on the initial ordering as well as compete on different time scales. Undulation instability is important in the transition kinetics in systems close to any phase boundary as shown for sphere- (section IV.A.2), cylinder- (section V.A.2), and lamellae-forming systems (section VI.A.1). In the only system far from any phase boundary (lamellae-forming system of section VI.A.2) defect movement is the only mechanism of alignment. In other systems defects may serve as nuclei of a new phase. We show an example of such a defect-mediated transition for a cylinder-forming system (section V.A.2). For spherical systems close to ODT (section IV.A.1) we observe partial melting as an intermediate stage.

Acknowledgment. Supercomputer time was provided by the Stichting Nationale Computer Faciliteiten (NCF). Jan Andzelm is thanked for very useful discussion.

References and Notes

(1) Hamley, I. W. *The Physics of Block Copolymers*; Oxford University Press: Oxford, 1998.
(2) Keller, A.; Pedemonte, E.; Willmouth, F. M. *Nature (London)* **1970**, *225*, 538.
(3) Thurn-Albrecht, T.; Schotter, J.; Kästle, G. A.; Emley, N.; Shibauchi, T.; Krusin-Elbaum, L.; Guarini, K.; Black, C. T.; Tuominen, M. T.; Russell, T. P. *Science* **2000**, *290*, 2126.
(4) Mansky, P.; DeRouchey, J.; Russell, T. P.; Mays, J.; Pitsikalis, M.; Morkved, T.; Jaeger, H. *Macromolecules* **1998**, *31*, 4399.
(5) Morkved, T. L.; Lu, M.; Urbas, A. M.; Ehrichs, E. E.; Jaeger, H. M.; Mansky, P.; Russell, T. P. *Science* **1996**, *273*, 931.
(6) Thurn-Albrecht, T.; Steiner, R.; DeRouchey, J.; Stafford, C.; Huang, E.; Bal, M.; Tuominen, M.; Hawker, C. J.; Russell, T. P. *Adv. Mater.* **2000**, *12*, 787.
(7) Hashimoto, T.; Bodycomb, J.; Funaki, Y.; Kimishima, K. *Macromolecules* **1999**, *32*, 952.
(8) Fasolka, M. J.; Mayes, A. M. *Annu. Rev. Mater. Res.* **2001**, *31*, 323.
(9) Knoll, A.; Horvat, A.; Lyakhova, K. S.; Krausch, G.; Sevink, G. J. A.; Zvelindovsky, A. V.; Magerle, R. *Phys. Rev. Lett.* **2002**, *89*, 035501.
(10) Knoll, A.; Lyakhova, K. S.; Horvat, A.; Krausch, G.; Sevink, G. J. A.; Zvelindovsky, A. V.; Magerle, R. *Nat. Mater.* **2004**, *3*, 886.
(11) Horvat, A.; Lyakhova, K. S.; Sevink, G. J. A.; Zvelindovsky, A. V.; Magerle, R. *J. Chem. Phys.* **2004**, *120*, 1117.
(12) Lyakhova, K. S.; Sevink, G. J. A.; Zvelindovsky. A. V.; Horvat, A.; Magerle, R. *J. Chem. Phys.* **2004**, *120*, 1127.
(13) Gurovich, E. *Macromolecules* **1994**, *27*, 7339.
(14) Gurovich, E. *Phys. Rev. Lett.* **1995**, *74*, 482.
(15) Onuki, A.; Fukuda, J. *Macromolecules* **1995**, *28*, 8788.
(16) Pereira, G. G.; Williams, D. R. M. *Macromolecules* **1999**, *32*, 8115.
(17) Ashok, B.; Muthukumar, M.; Russell, T. P. *J. Chem. Phys.* **2001**, *115*, 1559.
(18) Tsori, Y.; Andelman, D. *Int. Sci.* **2003**, *11*, 259.
(19) Tsori, Y.; Andelman, D. *Macromolecules* **2002**, *35*, 5161.
(20) Tsori, Y.; Tournilhac, F.; Andelman, D.; Leibler, L. *Phys. Rev. Lett.* **2003**, *90*, 145504.
(21) Lin, C.-Y.; Schick, M.; Andelman, D. *Macromolecules* **2005**, *38*, 5766.
(22) Amundson, K.; Helfand, E.; Davis, D. D.; Quan, X.; Patel, S. S. *Macromolecules* **1991**, *24*, 6546.
(23) Amundson, K.; Helfand, E.; Quan, X.; Smith, S. D. *Macromolecules* **1993**, *26*, 2698.
(24) Amundson, K.; Helfand, E.; Quan, X.; Hudson, S. D.; Smith, S. D. *Macromolecules* **1994**, *27*, 6559.
(25) Thurn-Albrecht, T.; DeRouchey, J.; Russell, T. P.; Jaeger, H. M. *Macromolecules* **2000**, *33*, 3250.
(26) Böker, A.; Elbs, H.; Hänsel, H.; Knoll, A.; Ludwigs, S.; Zettl, H.; Zvelindovsky, A. V.; Sevink, G. J. A.; Urban, V.; Abetz, V.; Müller A. H. E.; Krausch, G. *Macromolecules* **2003**, *36*, 8078.
(27) Xu, T.; Zvelindovsky, A. V.; Sevink, G. J. A.; Gang, O.; Ocko, B.; Zhu, Y. Q.; Gido, S. P.; Russell, T. P. *Macromolecules* **2004**, *37*, 6980. In this paper, the simulation polymer volume was miscalculated. The correct polymer volume is $v = 188$ nm^3.
(28) Zvelindovsky, A. V.; Sevink, G. J. A. *Phys. Rev. Lett.* **2003**, *90*, 049601.
(29) Taniguchi, T.; Sato, K.; Doi, M. In *Statistical Physics, CP 519*; Tokuyama, M., Stanley, H. E., Eds.; American Institute of Physics: Melville, NY, 2000; pp 581−583.
(30) Böker, A.; Elbs, H.; Hänsel, H.; Knoll, A.; Ludwigs, S.; Zettl, H.; Urban, V.; Abetz, V.; Müller, A. H. E.; Krausch, G. *Phys. Rev. Lett.* **2002**, *89*, 135502.
(31) Xu, T.; Zhu, Y.; Gido, S. P.; Russell, T. P. *Macromolecules* **2004**, *37*, 2625.
(32) Thurn-Albrecht, T.; DeRouchey, J.; Russell, T. P.; Kolb, R. *Macromolecules* **2002**, *35*, 8106.
(33) DeRouchey, J.; Thurn-Albrecht, T.; Russell, T. P.; Kolb, R. *Macromolecules* **2004**, *37*, 2538.
(34) Böker, A.; Abetz, V.; Krausch, G. *Phys. Rev. Lett.* **2003**, *90*, 049602.
(35) Schmidt, K.; Böker, A.; Zettl, H.; Schubert, F.; Hänsel, H.; Fischer, F.; Weiss, T. M.; Abetz, V.; Zvelindovsky, A. V.; Sevink, G. J. A.; Krausch, G. *Langmuir* **2005**, *21*, 11974.
(36) van Vlimmeren, B. A. C.; Maurits, N. M.; Zvelindovsky, A. V.; Sevink, G. J. A.; Fraaije, J. G. E. M. *Macromolecules* **1999**, *32*, 646.
(37) Onuki, A. *Phase Transition Dynamics*; Cambridge University Press: Cambridge, 2002.
(38) Kawakatsu, T. *Phys. Rev. E* **1997**, *56*, 3240; **1998**, *57*, 6214.

(39) Sevink, G. J. A.; Zvelindovsky, A. V.; van Vlimmeren, B. A. C.; Maurits, N. M.; Fraaije, J. G. E. M. *J. Chem. Phys.* **1999**, *110*, 2250.
(40) Landau, L. D.; Lifshitz, E. M. *Electrodynamics of Continuous Media*; Pergamon: Oxford, 1960.
(41) Landau, L. D.; Lifshitz, E. M. *Fluid Mechanics*; Pergamon: Oxford, 1987.
(42) Lin, Zh.; Kerle, T.; Russell, T. P.; Schäffer, E.; Steiner, U. *Macromolecules* **2002**, *35*, 3971.
(43) Feng, J.; Ruckenstein, E. *J. Chem. Phys.* **2004**, *121*, 1609.
(44) Pu, Y.; Rafailovich, M. H.; Sokolov, J.; Gersappe, D.; Peterson, T.; Wu, W.-L.; Schwarz, S. A. *Phys. Rev. Lett.* **2001**, *87*, 206101.
(45) Leibler, L. *Macromolecules* **1980**, *13*, 1602.
(46) Huinink, H. P.; van Dijk, M. A.; Brokken-Zijp, J. C. M.; Sevink, G. J. A. *Macromolecules* **2001**, *34*, 5325.
(47) Sevink, G. J. A.; Zvelindovsky, A. V. *J. Chem. Phys.* **2004**, *121*, 3864.
(48) Michielsen, K.; de Readt, H. *Phys. Rep.* **2001**, *347*, 461.
(49) Michielsen, K.; de Readt, H. *Comput. Phys. Commun.* **2000**, *132*, 94.
(50) Yokoyama, H.; Mates, T. E.; Kramer, E. J. *Macromolecules* **2000**, *33*, 1888.
(51) Xu, T.; Zvelindovsky, A. V.; Sevink, G. J. A.; Lyakhova, K. S.; Jinnai, H.; Russell, T. P. *Macromolecules* **2005**, *38*, 10788.
(52) Guo, H. X.; Kremer, K.; Soddemann, T. *Phys. Rev. E* **2002**, *66*, 061503.
(53) Böker, A.; Knoll, A.; Elbs, H.; Abetz, V.; Müller, A. H. E.; Krausch, G. *Macromolecules* **2002**, *35*, 1319.

MA060143R